Hidden Order in Spin-Liquid $Gd_3Ga_5O_{12}$

Joseph A. M. Paddison,[1,2] Henrik Jacobsen,[3,4] Oleg A. Petrenko,[5]
Maria Teresa Fernández-Díaz,[6] Pascale P. Deen,[3,4] Andrew L. Goodwin[1]

[1]Department of Chemistry, University of Oxford, Inorganic Chemistry Laboratory,
South Parks Road, Oxford OX1 3QR, U.K.
[2]ISIS Facility, Rutherford Appleton Laboratory, Chilton,
Didcot, Oxfordshire OX11 0QX, U.K.
[3]Nanoscience Center, Niels Bohr Institute, University of Copenhagen,
DK-2100 Copenhagen Ø, Denmark
[4]European Spallation Source, Tunavägen 24, Lund, Sweden
[5]Department of Physics, University of Warwick, Coventry, CV4 7AL, U.K.
[6]Institut Max von Laue–Paul Langevin, F-38042 Grenoble 9, France

E-mail: pascale.deen@esss.se.
E-mail: andrew.goodwin@chem.ox.ac.uk.

The search for new states of matter is a fundamental theme of condensed-matter science. Frustrated magnetic materials are promising candidates for new states because lattice geometry suppresses conventional magnetic dipole order, potentially allowing non-dipole ("hidden") order to emerge in its place. An image of a hidden-order state at the atomic scale has long been sought, but has proved difficult to obtain because microscopic probes are not directly sensitive to hidden order. Here, we develop an atomic-scale image of the spin-liquid state in the canonical frustrated magnet $Gd_3Ga_5O_{12}$. We further show that this state exhibits a hidden order which has three remarkable properties.

First, it is an emergent phenomenon, in which multipoles are formed from ten-spin loops. Second, it is long-range, with a diverging correlation length. Third, it is a consequence of the interplay between antiferromagnetic spin correlations and local magnetic anisotropy, which allows it to be indirectly observed in neutron-scattering experiments.

When a material undergoes a transition to an ordered state, its physical properties change. One of the greatest triumphs of twentieth-century physics was to explain these macroscopic changes in terms of the microscopic ordering of atoms and magnetic dipole moments (spins). A canonical example is antiferromagnetic order, which remained hidden until the development of neutron-scattering experiments in the 1940s (*1*). Today, a similar situation exists in "hidden order" materials, where the order is likely to be non-dipolar and therefore cannot be directly probed by our current experimental techniques (see, e.g., (*2–4*)). Hidden-order states are fascinating because they are qualitatively new states of matter. Exotic examples such as quantum spin nematics, chiral spin ices, and multipolar spin-orbital order have been theoretically proposed (*5–7*). Experimentally, the hidden-order challenge is twofold. First, we wish to discover new hidden-order materials beyond the canonical example of URu_2Si_2 (*2, 8*). Second, we require an atomic-scale image of a hidden-order state which takes full advantage of the indirect sensitivity afforded by modern experimental techniques.

Frustrated magnetic materials are promising candidates for the discovery of new hidden-order states (*9*). In frustrated systems, the lattice geometry suppresses conventional (long-range) spin order and a "spin liquid" phase may exist instead (*10*). Crucially, the strong spin correlations in spin-liquid states can lead to spin clusters behaving as a single object. This leads to the prospect that a property of spin clusters may show non-dipolar long-range order, even though individual spins remain in a liquid-like state (*11*). The experimental signature of a potential hidden order state is an anomaly in thermodynamic measurements which is not accompanied by a

transition to long-range or frozen spin order (indicated, e.g., by the development of magnetic Bragg peaks in neutron-diffraction experiments) (*2*). This anomaly may be either sharp, as in a conventional second-order phase transition, or broad, as for the transition from the paramagnetic phase to the "Coulomb phase" in spin-ice materials (*12*).

The well-studied frustrated magnet $Gd_3Ga_5O_{12}$ (gadolinium gallium garnet, GGG) exhibits thermodynamic anomalies of the second type. In GGG, a spin-liquid state is observed at temperatures above a spin-glass transition at $T_g \approx 0.14\,\mathrm{K}$ (*13*). Evidence for a conventional spin liquid in GGG is the suppression of T_g to temperatures far below the antiferromagnetic interaction strength of $\sim$2 K (*14–16*), the observation of liquid-like magnetic diffuse scattering in powder neutron-scattering measurements (*17*), and the persistence of strong spin fluctuations to low temperature (*18–20*). Yet, broad anomalies are present in both the non-linear susceptibility χ_3 and the magnetic specific heat at around $0.5\,\mathrm{K}$, which do not yet have a well-understood microscopic origin (*13, 21*).

The crystal structure of GGG is shown in Fig. 1(a). The unit cell is cubic and contains 24 equivalent magnetic Gd^{3+} ions ($S = 7/2$, $L = 0$). The Gd^{3+} ions form two interpenetrating networks of opposite chirality, each of which describes a three-dimensional arrangement of corner-sharing triangles known as hyperkagome. The local environment of the Gd^{3+} ions is shown in Fig. 1(b), where local axes $\mathbf{x}, \mathbf{y}, \mathbf{z}$ are defined by the three two-fold rotational axes of point symmetry. Of particular importance in the GGG structure are the ten-spin loops shown in blue in Fig. 1(b), which are the shortest path connecting a Gd^{3+} ion back to itself beyond individual triangles. Each Gd^{3+} also sits in the middle of exactly one loop; hence loop and atom share the same point symmetry and the local axes defined for atoms apply equally to loops. In a simple model which considers only nearest-neighbour antiferromagnetic interactions, collective rotations of the loop spins allow the system to move at no energy cost between its degenerate ground states (*22*). We therefore anticipate that the ten-spin loops should play a key role in any

emergent behaviour present in the spin-liquid state.

We performed single-crystal neutron-scattering measurements on GGG in order to probe the spin-liquid state. These measurements are challenging because of the very large neutron absorption cross-section of natural Gd, and a high-energy incident neutron beam was used to mitigate against this problem (see Materials and Methods). The left-hand panels of Fig. 2(a) show single-crystal neutron-scattering data at $T = 0.175$ K. In order to model these highly-structured magnetic diffuse-scattering data, we use the reverse Monte Carlo method (*23, 24*) to perform quantitative refinement to magnetic diffuse-scattering data from Ref. (*17*), which were collected on a powder sample (see Materials and Methods). The RMC method has two important properties: it generates an atomic-scale model from which arbitrary (non-dipolar) correlation functions can be calculated, and it does not introduce a predetermined set of magnetic interactions which could bias the results (*25*). Excellent agreement between the RMC fit and the powder data is achieved at $T = 0.175$ K [Fig. 2(b)]. Calculations of the single-crystal scattering from the refined RMC model show close qualitative agreement with the experimental single-crystal data, which provides evidence for the validity of the RMC model [Fig. 2(a), right panels]. Consistent with Mössbauer measurements (*26*), we obtain a strongly anisotropic distribution of spin orientations with spins preferentially oriented within their local xy planes [Fig. 2(b), inset]. Our RMC refinements do not determine the microscopic origin of this xy anisotropy. However, additional simulations of the state-of-the-art spin Hamiltonian for GGG (*15, 16*) showed that the magnetic dipolar interaction (which couples spin and space degrees of freedom) generates the same xy anisotropy (see SI). The sensitivity of the powder-averaged data to local spin anisotropy was confirmed by showing that an isotropic model does not fit the data successfully [green line in Fig. 2(b)]. Consistent with simulations (*27*), the radial spin correlation function $\langle \mathbf{S}(0) \cdot \mathbf{S}(r) \rangle$ reveals a rapid decay of spin correlations with an exponential correlation length $\xi = 4.951(2)$ Å (similar to the nearest-neighbour distance $r_{\mathrm{nn}} = 3.78$ Å) and a

nearest-neighbour spin correlation coefficient $\langle \mathbf{S}(0) \cdot \mathbf{S}(r_{\mathrm{nn}}) \rangle$ close to -0.5 [Fig. 2(c)]. The temperature-dependence of ξ was obtained from fits to powder diffuse scattering data at higher temperatures (see SI) and shows a gradual decrease with increasing temperature [Fig. 2(c), inset]. Based on this analysis, we conclude that the spin anisotropy and short-range *dipole* order of our model are consistent with expectations.

To look for exotic behaviour beyond dipole order, we consider the ten-ion loops which are shown in Fig. 3(a). Adjacent spins in a loop are nearest neighbours and are therefore antiferromagnetically correlated. Surprisingly, inspection of spin configurations suggested that significant antiferromagnetic alignment persists beyond nearest neighbours and throughout the loop, a result obscured by the radial average in Fig. 2(c). To quantify this correlation, we calculate the average spin alignment axis of each loop,

$$\mathbf{L}(\mathbf{r}) = \frac{1}{10} \sum_{n} \cos(n\pi) \mathbf{S}_n(\mathbf{r}), \tag{1}$$

where $\mathbf{r}$ is the position of the centre of the loop and $\mathbf{S}_n$ are unit-length spins within the loop ($n \in \{1, ..., 10\}$). We refer to $\mathbf{L}(\mathbf{r})$ as the "ten-spin director" to emphasise that $\mathbf{L}$ does not transform as a vector, because the two-fold symmetry symmetry of the Gd^{3+} site requires that both $\mathbf{L}(\mathbf{r})$ and $-\mathbf{L}(\mathbf{r})$ identify the same alignment axis (our use of the director here mirrors the description of nematic liquid crystals (*28*)). The average magnitude $\langle |\mathbf{L}(\mathbf{r})| \rangle = 0.49$ with standard deviation 0.18, which shows that antiferromagnetic correlation is strong within each loop and relatively consistent between different loops. The cyclic arrangement of ten antiferromagnetic spins in a ring describes a multipole of order 6, which contains 5 nodal planes orthogonal to the plane of the loop and a single nodal plane coincident with it [Fig. 3(a)]. Viewed in these terms, the normalised ten-spin director $\hat{\mathbf{L}} = \mathbf{L}/|\mathbf{L}|$ describes the multipole orientation associated with a given ten-ion loop. Fig. 3(b) shows our key result: the distribution of normalised ten-spin directors is strongly peaked along the local $\mathbf{z}$ axis. This result is remarkable because

it shows that the fluctuations of the ten spins in a loop select a single axis on average, so the rotational degree of freedom possessed by xy-like spins is lost in the loop directors. Hence the ten-spin directors have no ground-state degrees of freedom, and are ordered, with excitations normal to the local $\mathbf{z}$ axis [Fig. 3(b)]. Moreover, since the ten-spin directors describe multipole orientations, the order is multipolar. The unit cell of this magnetic multipole crystal is shown in Fig. 3(c). The multipole order preserves the symmetry of the crystal structure but is not required by this symmetry, which only constrains the distribution of ten-spin directors to preserve the three two-fold rotation axes. Fig. 3(d) shows the axial correlation function of the normalised ten-spin directors,

$$g_{\mathrm{L}}(r) = 2\left\langle |\hat{\mathbf{L}}(0)\cdot\hat{\mathbf{L}}(r)|\right\rangle - 1, \tag{2}$$

which is equal to -1 if, on average, loop directors separated by distance r are normal and to $+1$ if they are collinear. The correlation length of this function diverges within the statistical error of our refinements (see SI), as is to be expected from the axial distribution of ten-spin directors in Fig. 3(b). Analogous to a non-collinear antiferromagnet, the non-collinearity of local $\mathbf{z}$ axes for different loops leads to $g_{\mathrm{L}}(r)$ taking several values, but does not affect the divergence of the correlation length.

How is our analysis sensitive to non-dipolar order, given that neutron scattering is a dipolar probe? To answer this question we note that neutron scattering is directly sensitive to two quantities: the spin anisotropy and the spin-pair correlations (*29*). If an interplay of both quantities generates hidden order, neutron scattering may be indirectly sensitive to the hidden order itself. We performed Monte Carlo simulations which show that this is the case for GGG: long-range multipole order is present when both xy anisotropy and antiferromagnetic interactions are included, but is absent for either (i) isotropic antiferromagnetic interactions or (ii) noninteracting spins with xy anisotropy (see SI). Hence, hidden order is not a trivial consequence of either xy anisotropy or antiferromagnetic interactions alone.

The development of hidden order provides a plausible explanation for observed thermodynamic anomalies in the spin-liquid state of GGG. We show this by considering a simple model in which spins are constrained to lie in their local xy planes and are coupled by antiferromagnetic nearest-neighbour interactions. We do not claim that this xy model accurately represents the spin Hamiltonian of GGG, but consider it instead because it is the simplest model showing the hidden-order state. From this model we calculate two quantities: the magnetic specific heat C_{mag}, and a limiting multipole correlation g_{max}, which we determine by fitting a straight line to $g_{\mathrm{L}}(r)$ at the distances where it takes its maximum value for the multipole crystal—*i.e.*, the distances separating loops which share the same local axes [Fig. 3(d)]. Fig. 3(e) compares the broad peak in the specific heat and g_{max} determined from the xy model with the experimental specific-heat peak and g_{max} determined from RMC refinement. We make three key observations. First, a broad specific-heat peak occurs in the xy model and the real material, which both show hidden order; moreover, this specific-heat peak is absent for models without hidden order (see SI). Second, there is a large change in g_{max} over the temperature range where the specific-heat peak develops, but only a much smaller change in the spin correlation length [Fig. 2(c), inset]. Third, the temperature evolution of the specific-heat peak correlates with the evolution of hidden order in a similar way for both xy model and experiment [Fig. 3(e)]. These results suggest that the broad specific-heat anomaly is a signature of loss of entropy associated with the developing hidden order.

The hidden-order state of GGG is the only known example of a magnetic multipole crystal in a spin liquid. This hidden-order state does not break the crystal symmetry and is built from groups of spins which are individually fluctuating in space and time (*18–20*); examples of how spin fluctuations occur consistently with multipolar order are shown in the SI. It is also likely that the multipolar order will be apparent in larger clusters than the ten-spin loops. Compared to the canonical example of URu_2Si_2 (*2*), the lack of symmetry-breaking in GGG broadens

the specific-heat anomaly observed as the hidden-order state develops, similar to the transition to the "Coulomb phase" in spin-ice materials (*12*). An interesting comparison can be drawn with frustrated spinels such as $MgCr_2O_4$, in which hexagonal spin loops may form strongly-ordered ("protected") degrees of freedom but adjacent loops are only weakly correlated (*30, 31*). The hidden order in GGG represents the opposite limit, in which the loops are long-range ordered while individual spins show only short-range correlations. The case of GGG therefore represents a new realisation of hidden order, with fundamentally-different properties to previous examples. Our results suggest that the atomic-scale refinement approach used here will prove valuable to unmask hidden-order states in other materials, such as chiral-spin-liquids in frustrated magnetic materials (*11*) and spin-nematics in high-temperature superconductors (*32*).

Materials and methods. Single-crystal neutron-scattering measurements were performed using the hot-neutron four-circle diffractometer D9 at the Institut Laue–Langevin. The sample was a $1 \times 1 \times 3$ mm^3 single crystal of GGG which was grown for the laser industry by Princeton Scientific using the Czochralski method with an Ir crucible under an Ar atmosphere. The crystal is not isotope-enriched and thus contains a large amount of the highly neutron-absorbing isotopes ^{155}Gd and ^{157}Gd. An incident neutron wavelength $\lambda = 0.512\,$Å was used to minimise neutron absorption, which is greatly reduced for $\lambda < 0.6\,$Å (*33*). As a consequence of the short λ, regions of reciprocal space for which $Q \leq 0.98\,\text{Å}^{-1}$ could not be accessed in the experiment. Data were therefore collected over the range $0.98 < Q < 3.77\,\text{Å}^{-1}$. The sample was held in a Cu foil pocket, cooled using a dilution fridge, and the neutron-scattering intensity was measured at $T = 10\,$K and $T = 0.175\,$K. The magnetic scattering intensity was isolated by taking the difference of these two datasets and the $m\bar{3}m$ diffraction symmetry appropriate for GGG was applied to the data. Reverse Monte Carlo refinements to powder diffuse-scattering data from Ref. (*17*) were performed with a model of size $6 \times 6 \times 6$ crystallographic unit cells

(5184 spins) using periodic boundary conditions and were initialised from random starting configurations. Calculated quantities were averaged over 20 independent RMC configurations to minimise statistical noise. Technical details of the RMC refinements are given in SI.

References and Notes

1. C. G. Shull, J. S. Smart, *Phys. Rev.* **76**, 1256 (1949).
2. J. A. Mydosh, P. M. Oppeneer, *Rev. Mod. Phys.* **83**, 1301 (2011).
3. P. Santini, S. Carretta, N. Magnani, G. Amoretti, R. Caciuffo, *Phys. Rev. Lett.* **97**, 207203 (2006).
4. S. Chakravarty, R. B. Laughlin, D. K. Morr, C. Nayak, *Phys. Rev. B* **63**, 094503 (2001).
5. P. Chandra, P. Coleman, *Phys. Rev. Lett.* **66**, 100 (1991).
6. S. Onoda, Y. Tanaka, *Phys. Rev. Lett.* **105**, 047201 (2010).
7. H. Ikeda, *et al.*, *Nat. Phys.* **8**, 528 (2012).
8. E. Ressouche, *et al.*, *Phys. Rev. Lett.* **109**, 067202 (2012).
9. J. T. Chalker, P. C. W. Holdsworth, E. F. Shender, *Phys. Rev. Lett.* **68**, 855 (1992).
10. R. Moessner, A. P. Ramirez, *Physics Today* **59**, 24 (2006).
11. Y. Machida, S. Nakatsuji, S. Onoda, T. Tayama, T. Sakakibara, *Nature* **463**, 210 (2010).
12. R. G. Melko, M. J. P. Gingras, *J. Phys.: Condens. Matter* **16**, R1277 (2004).
13. P. Schiffer, *et al.*, *Phys. Rev. Lett.* **74**, 2379 (1995).
14. W. Kinney, W. Wolf, *J. Appl. Phys.* **50**, 2115 (1979).

15. T. Yavors'kii, M. Enjalran, M. J. P. Gingras, *Phys. Rev. Lett.* **97**, 267203 (2006).

16. N. d'Ambrumenil, O. A. Petrenko, H. Mutka, P. P. Deen, *arXiv:1501.03493 (Phys. Rev. Lett., accepted)* (2015).

17. O. A. Petrenko, C. Ritter, M. Yethiraj, D. McK Paul, *Phys. Rev. Lett.* **80**, 4570 (1998).

18. P. P. Deen, *et al.*, *Phys. Rev. B* **82**, 174408 (2010).

19. I. M. Marshall, *et al.*, *J. Phys.: Cond. Matt.* **14**, L157 (2002).

20. S. R. Dunsiger, *et al.*, *Phys. Rev. Lett.* **85**, 3504 (2000).

21. J. A. Quilliam, *et al.*, *Phys. Rev. B* **87**, 174421 (2013).

22. S. Ghosh, T. F. Rosenbaum, G. Aeppli, *Phys. Rev. Lett.* **101**, 157205 (2008).

23. R. L. McGreevy, L. Pusztai, *Mol. Simul.* **1**, 359 (1988).

24. J. A. M. Paddison, A. L. Goodwin, *Phys. Rev. Lett.* **108**, 017204 (2012).

25. J. A. M. Paddison, J. R. Stewart, A. L. Goodwin, *J. Phys.: Condens. Matter* **25**, 454220 (2013).

26. P. Bonville, J. A. Hodges, J. P. Sanchez, P. Vulliet, *Phys. Rev. Lett.* **92**, 167202 (2004).

27. O. A. Petrenko, D. McK. Paul, *Phys. Rev. B* **63**, 024409 (2000).

28. R. W. Ruhwandl, E. M. Terentjev, *Phys. Rev. E* **56**, 5561 (1997).

29. G. L. Squires, *Introduction to the theory of thermal neutron scattering* (Cambridge University Press, 1978).

30. S.-H. Lee, *et al.*, *Nature* **418**, 856 (2002).

31. K. Tomiyasu, *et al.*, *Phys. Rev. Lett.* **110**, 077205 (2013).

32. C. V. Parker, *et al.*, *Nature* **468**, 677 (2010).

33. G. Leinweber, *et al.*, *Nuc. Sci. Eng.* **154**, 261 (2006).

34. We thank S. A. Hall, M. E. Zhitomirsky, N. d'Ambrumenil, J. R. Stewart, M. J. P. Gingras, T. Yavors'kii, S. E. Dutton, M. Mourigal, W. J. K. Fletcher and M. J. Cliffe for useful discussions, O. Young and S. Holm for assistance with the early experimental work, and the staff at the ILL for experimental support. P.P.D. and H.J. gratefully acknowledge financial support from the Danish Research Council for Nature and Universe through DANSCATT. J.A.M.P. and A.L.G. gratefully acknowledge financial support from the STFC, EPSRC (EP/G004528/2), and ERC (No. 279705).

Fig. 1.

Crystallographic properties of GGG. (a) Crystal structure of GGG, showing only magnetic Gd^{3+} ions. The two interpenetrating networks of corner-sharing triangles are coloured red and blue. (b) Local environment of Gd^{3+} ions. The local axes $\mathbf{x}, \mathbf{y}, \mathbf{z}$ are defined by the three two-fold axes of point symmetry of the Gd^{3+} site: $\mathbf{x} \in \langle 100 \rangle$ and $\mathbf{y}, \mathbf{z} \in \frac{1}{\sqrt{2}}\langle 110 \rangle$, where $\mathbf{z}$ is chosen to pass through the centres of the two triangles which contain the Gd^{3+} ion. Each Gd^{3+} ion is located at the centre of a loop of ten Gd^{3+} ions from the other network, where the mean plane of the loop is perpendicular to the local $\mathbf{z}$ axis.

Fig. 2.

Experimental data, fits, and calculations for GGG at $T = 0.175\,\mathrm{K}$. (a) Magnetic diffuse scattering in two reciprocal-space planes. The upper image shows the $(hk0)$ plane and the lower image shows the (hkk) plane. In each image, the left-hand panel shows experimental data and the right-hand panel shows the calculation from reverse Monte Carlo (RMC) refinements described in the text. Regions where there are no data are shown in white. (b) RMC fit to powder diffuse-scattering data (from Ref. (*17*)). Data are shown as black circles, fit as a red line, and difference (fit–data) as a blue line. The scattering function calculated from the alternative isotropic model described in the text is shown as a green line. The inset shows a stereographic projection of the logarithmic probability distribution $\ln(p)$ of spin orientations (defined in the SI), revealing preferential spin alignment in the local xy plane [Fig. 1(b)]. (c) Radial spin correlation function. The bars show spin correlation values and the solid black line shows a fit to an exponential envelope, $\pm\exp(-r/\xi)$, where $\xi = 4.951(2)\,\text{Å}$. Correlations with positive (ferromagnetic) values are shown in orange and correlation with negative (antiferromagnetic) values are shown in green. The inset shows the temperature-dependence of ξ (the solid line is a guide to the eye). Error bars in (c) are smaller than the line thickness or symbol size in the plots.

Fig. 3.

Multipole order in GGG. (a) Relationship between representative spin orientations and ten-spin director for a ten-spin loop. Antiferromagnetically-correlated spins are coloured alternating green and orange as the loop is traversed. The multipole formed by the ten spins is shown at the centre of the loop, and the ten-spin director defined in the text is shown as a red double-headed arrow. (b) Stereographic projection showing that the logarithmic probability distribution function $\ln(p)$ of normalised ten-spin directors (defined in the SI) is strongly peaked along the local **z** axis (shown by the red double-headed arrow in (a)). Fluctuations of the loop director normal to **z** are also apparent. (c) Crystal structure showing the unit cell of the magnetic multipole crystal. Multipoles and ten-spin directors are shown as in (a) and are illustrated for only one of the two networks for clarity. (d) Axial correlation function of normalised ten-spin directors, showing the presence of long-range multipole order. Collinear correlations are shown as orange bars and normal correlations are shown as green bars. (e) Temperature evolution of the broad peak in the magnetic specific heat ΔC (black symbols) compared with temperature evolution of the limiting multipole correlation $g_{\max}$ (orange symbols). Solid circles show experimental specific-heat data (from Ref. (*13*)) and $g_{\max}$ obtained from RMC refinement to experimental neutron-scattering data, while open squares show specific heat and $g_{\max}$ calculated for a model with antiferromagnetic nearest-neighbour interactions and xy anisotropy as described in the text. The broad specific-heat peak has been isolated by fitting polynomial background functions to the experimental specific-heat data and model calculation (see SI).

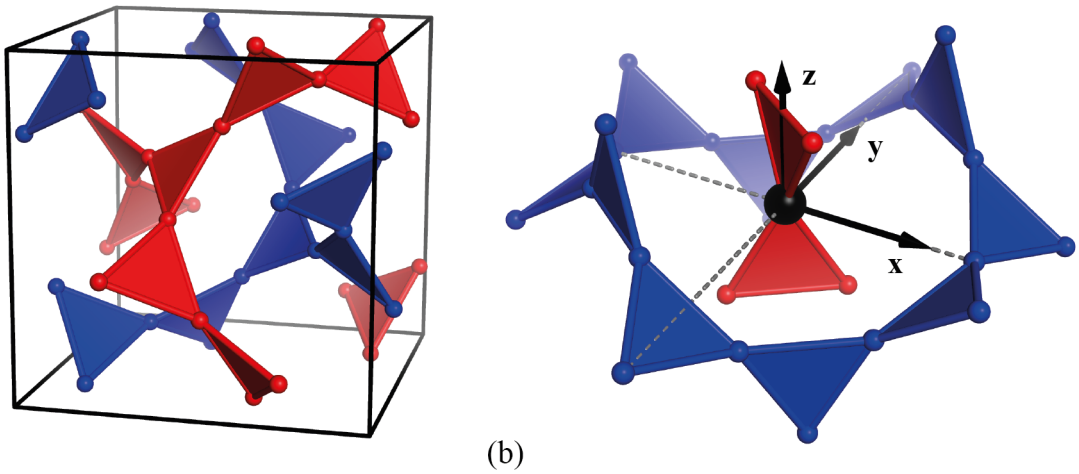

(a) (b)

FIGURE 1

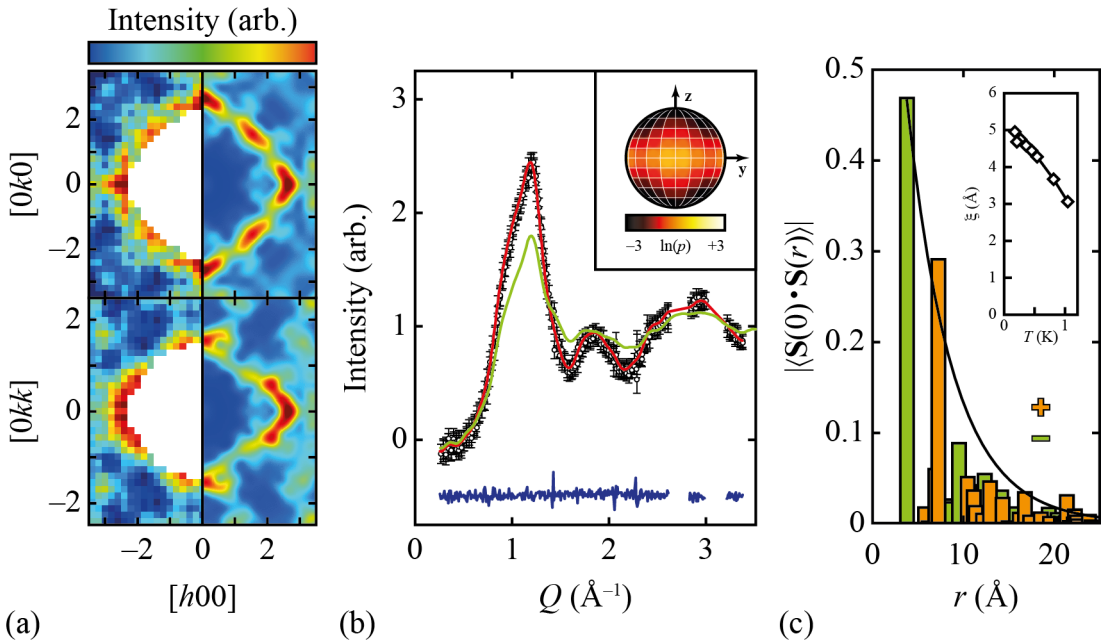
Intensity (arb.)
[0k0]
[0kk]
[h00]
(a)
Intensity (arb.)
Q (Å⁻¹)
z
y
−3 ln(p) +3
(b)
|⟨S(0)•S(r)⟩|
r (Å)
ξ (Å)
T (K)
(c)

FIGURE 2

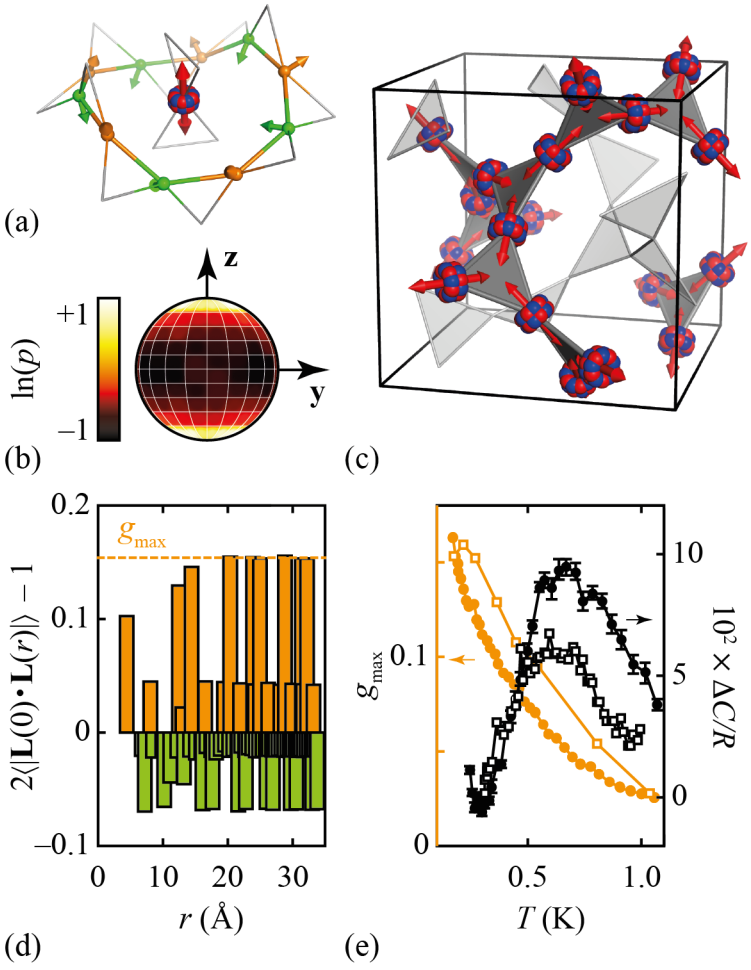
(a)
z
+1
ln(p)
–1
y
(b)
(c)
0.2
0.1
0
–0.1
g_{max}
$2\langle|\mathbf{L}(0)\cdot\mathbf{L}(r)|\rangle - 1$
0
10
20
30
r (Å)
(d)
g_{max}
0.1
0
10
5
0
$10^2 \times \Delta C/R$
0.5
1.0
T (K)
(e)

FIGURE 3